

Monolayer/bilayer transition in Langmuir films of derivatized gold nanoparticles at the gas/water interface: An x-ray scattering study

Masafumi Fukuto, Ralf K. Heilmann,^{a)} and Peter S. Pershan

Department of Physics and Division of Engineering and Applied Sciences, Harvard University, Cambridge, Massachusetts 02138

Antonella Badia

Department of Chemistry, Université de Montréal, Montreal, Canada

R. Bruce Lennox

Department of Chemistry, McGill University, 801 Sherbrooke St. W., Montreal H3A 2K6, Canada

(Received 3 September 2003; accepted 17 November 2003)

The microscopic structure of Langmuir films of derivatized gold nanoparticles has been studied as a function of area/particle on the water surface. The molecules (AuSHDA) consist of gold particles of mean core diameter $D \sim 22 \text{ \AA}$ that have been stabilized by attachment of carboxylic acid terminated alkylthiols, $\text{HS}-(\text{CH}_2)_{15}-\text{COOH}$. Compression of the film results in a broad plateau of finite pressure in the surface pressure versus area/particle isotherm that is consistent with a first-order monolayer/bilayer transition. X-ray specular reflectivity (XR) and grazing incidence diffraction show that when first spread at large area/particle, AuSHDA particles aggregate two dimensionally to form hexagonally packed monolayer domains at a nearest-neighbor distance of $a = 34 \text{ \AA}$. The lateral positional correlations associated with the two-dimensional (2D) hexagonal order are of short range and extend over only a few interparticle distances; this appears to be a result of the polydispersity in particle size. Subsequent compression of the film increases the surface coverage by the monolayer but has little effect on the interparticle distance in the close-packed domains. The XR and off-specular diffuse scattering (XOSDS) results near the onset of the monolayer/bilayer coexistence plateau are consistent with complete surface coverage by a laterally homogeneous monolayer of AuSHDA particles. On the high-density side of the plateau, the electron-density profile extracted from XR clearly shows the formation of a bilayer in which the newly formed second layer on top is slightly less dense than the first layer. In contrast to the case of the homogeneous monolayer, the XOSDS intensities observed from the bilayer are higher than the prediction based on the capillary wave model and the assumption of homogeneity, indicating the presence of lateral density inhomogeneities in the bilayer. According to the results of Bragg rod measurements, the 2D hexagonal order in the two layers of the bilayer are only partially correlated.

© 2004 American Institute of Physics. [DOI: 10.1063/1.1640334]

I. INTRODUCTION

Chemically synthesized metallic and semiconductor nanoparticles have received a great deal of attention in recent years. Interest in such particles originates from the fact that due to their small sizes, which typically range from ~ 10 to $\sim 100 \text{ \AA}$, the effects of finite size or “confinement” play an essential role in determining their electronic, optical, and other physical properties.^{1–7} Nanoparticles also serve as building blocks for new materials and devices, and many studies have been directed toward exploiting their unique size-dependent properties in practical applications, e.g., in micro- or nanoelectronics, optoelectronics, chemical and biosensors, and catalysis.^{5–14} One of the challenges in this field of research is to find ways to organize nanoparticles into microscopically well-defined structures, both three dimensional (3D) and two dimensional (2D), that are useful for some of those applications.^{6–9,15–19}

In the much-studied case of 2D structures involving ligand-protected nanoparticles, a variety of different methods have been developed to form a monolayer on a substrate. Most of the techniques utilize, in one way or another, the solubility of these particles in organic solvents or even in aqueous solutions in some cases.^{8,20} Another common feature is that a monolayer is initially formed at an interface with liquid, i.e., at a liquid/solid, liquid/vapor, or liquid/liquid interface. The simplest approach is to deposit nanoparticles directly from a solution onto a solid substrate, either by allowing drops to wet and evaporate on the substrate or by dipping the substrate in the solution to allow nanoparticles to self-assemble at the interface.^{8–10,17–19,21–33} The substrates used include pretreated surfaces that are coated by a self-assembled monolayer of organic molecules and are terminated with specific end groups.^{8,9,18,19,21–24} Another approach is to spread the solution on the water surface to form a Langmuir monolayer, which then can be transferred onto a solid substrate by using either Langmuir–Blodgett (LB) or Langmuir–Schaeffer (i.e., “stamping”) techniques.^{18,20,34–42}

^{a)}Present address: Space Nanotechnology Laboratory, Center for Space Research, Massachusetts Institute of Technology, Cambridge, MA 02139.

One important advantage of the Langmuir method is the ability to control the surface coverage. It may also be possible to control the interparticle spacing if the initial microscopic packing density can be further increased by laterally compressing the film. One of the more complex methods that have been used is based on attractive interactions between colloidal nanoparticles in an aqueous solution and a charged surfactant monolayer at the solution/air interface.^{20,43–48} In this approach, nanoparticles form a monolayer of their own just below the surfactant monolayer, and the composite film thus formed is transferred onto a solid support by the LB method. Finally, more recent studies have explored the formation of nanoparticle monolayers at liquid/liquid interfaces,^{49–51} and some of these films have also been transferred onto solid substrates.^{49,50}

One of the most commonly studied classes of metallic nanoparticles consists of colloidal gold or silver crystallites that are nucleated and grown from metallic ions in solution and are stabilized by simultaneous attachments of alkanethiols $\text{HS}-(\text{CH}_2)_{n-1}-\text{CH}_3$ (or thiol derivatives) onto their surface (denoted as “AuSCn” or “AgSCn”).^{3,4,29–37,52–62} Evidence that a 2D assembly of this class of nanoparticles may exhibit an interesting *collective* behavior under certain conditions has been provided by the recent studies of Langmuir films by Heath and co-workers.^{3,4,34–37,52,53} Their samples consisted of AuSCn ($n=9,12,18$) and AgSCn ($n=3,5,6,8,10,12$) particles with mean metal-core diameters D ranging from 18 to 80 Å. Their TEM images of transferred Langmuir-Schaeffer films indicate that in compressed monolayers AuSCn and AgSCn particles form close-packed structures with local 2D hexagonal order.^{34,35} They also measured the optical response of AgSCn monolayers at the air/water interface as a function of compression or the edge-to-edge separation δ between adjacent Ag cores. Their results show that compression leads to a sharp and discontinuous drop in both the linear reflectance and the nonlinear second-harmonic signal when the ratio δ/D falls below $\sim 20\%$ (or $\delta \sim 5$ Å for $D = 27$ Å).³⁵ They interpreted this as evidence for a 2D metal/insulator transition, attributing the observed effect to delocalization of electrons caused by sufficient overlap between electronic wave functions of adjacent particles.^{3,35,53} This interpretation was later supported by measurements of the complex low-frequency impedance^{52,53} and the complex optical dielectric function^{4,53} for monolayers on water and by the density of states extracted from scanning tunnel microscope (STM) measurements on transferred films.^{36,37,53} Each of the probed quantities exhibited metallic characteristics at small δ and behaved like an insulator at large δ ; moreover, the results were reversible with respect to the degree of compression.

The collapse of AuSCn and AgSCn monolayers at high surface pressure has also been studied, but to a much lesser extent. On the basis of their TEM images and the dependence $d\Pi_c/dT < 0$ of the collapse pressure Π_c on temperature, Heath *et al.* concluded that collapsed films are more disordered than the close-packed monolayer.^{34,35} They assumed that the collapsed film consisted of coexisting monolayer and bilayer regions. The recent optical study by Heinrichs *et al.* further showed that the monolayer collapse is also

associated with reduction in the metallic character of the film.⁴ They attribute the effect to increased structural disorder in the collapsed bilayer, which tends to induce localization of electronic states.^{63,64}

This paper presents synchrotron x-ray scattering structural studies of Langmuir films of gold nanoparticles that are derivatized with carboxylic acid-terminated alkylthiol chains $\text{HS}-(\text{CH}_2)_{15}-\text{COOH}$ (“AuSHDA” with “HDA” denoting *hexadecanoic acid*). These particles differ from the more common AuSCn mentioned above in that instead of the hydrophobic $-\text{CH}_3$ group, the hydrophilic $-\text{COOH}$ group is exposed at the periphery. The surface pressure (Π) vs area/particle (A) isotherms of AuSHDA films at room temperature (25 °C) display clear signatures that are consistent with a first-order monolayer/bilayer transition. The microscopic structures on both sides of this transition have been probed in detail using x-ray specular reflectivity (XR), grazing incidence diffraction (GID), and off-specular diffuse scattering (XOSDS) techniques.

This paper is organized as follows: Section II describes relevant experimental details, Sec. III presents the results of Π - A isotherm, XR, XOSDS, and GID measurements, and Sec. IV summarizes the main conclusions.

II. EXPERIMENTAL DETAILS

A. Sample and Π - A isotherm measurements

The AuSHDA sample consisted of polydisperse gold nanoparticles derivatized with carboxylic acid-terminated hexadecanethiol chains $\text{HS}-(\text{CH}_2)_{15}-\text{COOH}$. The thiol terminus is chemically bonded to the surface of Au nanoparticles. The synthetic procedures have been described previously.^{55,56,58,61} A TEM study by Badia and co-workers⁵⁸ demonstrated that the synthesis produces polydisperse Au nanoparticles of typical mean Au-core diameter D in the range 20–30 Å with a typical standard deviation for the size distribution of $\Delta D \sim \pm 4-8$ Å (or $\Delta D/D = 20-30\%$). As will be described further in Sec. III, the x-ray measurements in the present study provided three independent measures of D in the actual AuSHDA sample that we used: (i) $D_l = 20.5$ Å, based on the monolayer thickness obtained from XR; (ii) $D_\phi = 22$ Å, based on the combination of the XR-based electron density in the monolayer and the microscopic area/particle extracted from the observed GID peaks; and (iii) $D_{\text{BR}} = 23.2$ Å, based on Bragg-rod measurements. We assume that the average of these three x-ray-based values, $\bar{D} \pm \delta\bar{D} = 22 \pm 1.4$ Å, is representative of the mean Au-core diameter of the actual sample, where $\delta\bar{D}$ refers to the uncertainty in the mean (to be distinguished from the standard deviation ΔD of the size distribution). The average molecular weight (MW) of AuSHDA, which is needed to calculate the number of particles spread on the wafer surface, was estimated as follows. For simplicity, we represent the Au core by a sphere of diameter $\bar{D} = 22 (\pm 1.4)$ Å and assume that on the core surface each thiol chain occupies an area of $A_{\text{thiol}} = 21.4$ Å², which is equal to the value found in self-assembled monolayers of thiols on planar Au(111) surfaces.^{34,54} Such a AuSHDA particle consists of 320 (± 62) Au atoms and 70 (± 9) thiol chains, and the corre-

sponding MW is equal to 83 200 g/mole ($\pm 12\,500$ g/mole or $\pm 15\%$). This value of MW was used to estimate the number of particles spread from solution onto the surface of the Langmuir trough. The area per particle A in the reported Π - A isotherms is equal to the ratio of the available trough surface area to this number. From the uncertainty in the MW, we estimate the uncertainty in the isotherm area A to be about $\delta A/A \sim \pm 15\%$.

Details on the Langmuir trough that was used in the present study have been described previously.^{65–67} A Teflon trough and a Wilhelmy-type surface pressure balance are enclosed in a sealed aluminum box. For isotherm measurements, the box was filled with high-purity N_2 gas. For x-ray measurements, high-purity He gas was used instead in order to reduce background scattering from gas in the beam path. All the measurements to be reported here were carried out at $T = 25.0^\circ\text{C}$. An aqueous solution which was preadjusted to $pH = 3$ by adding an appropriate amount of HCl (J. T. Baker, ULTREX II ultra pure reagent) to pure water (Milli-Q quality) was used both as the subphase and for flushing of the trough prior to spreading of a film. The acidic subphase was chosen to prevent ionization of the carboxylic acid groups. The spreading solution was prepared by dissolving a dry sample of AuSHDA particles in benzene (Sigma, HPLC grade); the nominal concentration of the solutions that were used ranged from 1.45 to 1.66 mg/mL. A film was deposited on the surface by spreading a measured volume of the solution, which ranged from 90 to 130 μL and corresponded to an initial, as-spread area of $A > 1300 \text{ \AA}^2/\text{particle}$.

Π - A isotherms were measured by using two different methods. In a stepwise continuous scan, each compression step (typically, $\Delta A = 6.5 \text{ \AA}^2/\text{particle}$ per step) was followed by a 15-sec wait, a measurement of surface pressure Π , and the next compression step. In a relaxation scan,^{65–67} the film was allowed to relax after each compression step ($\Delta A = 26 \text{ \AA}^2/\text{particle}$ per step); at each area A , the surface pressure was monitored every minute during relaxation until the pressure change over 5 min was less than 0.05 dyne/cm, at which point a final pressure was recorded and the film was compressed to the next area. For both methods, the barrier speed that was used for film compression corresponded to a compression rate of $dA/dt = 0.65 (\text{ \AA}^2/\text{particle})/\text{s}$. For x-ray experiments, the film was compressed using the stepwise continuous method, but it was allowed to relax once the target area was reached. X-ray measurements were initiated only after the surface pressure had relaxed to the value given by the relaxation isotherm.

B. X-ray measurements

X-ray experiments were carried out at the Beamline X22B of the National Synchrotron Light Source, using the Harvard/BNL liquid surface spectrometer⁶⁵ operated at an x-ray wavelength of $\lambda = 1.55 \text{ \AA}$. The relationships between the surface (the x - y plane) and the scattering angles (α , β , 2θ) are illustrated in Fig. 1. The difference between the scattered and incident wave vectors defines the wave vector transfer $\mathbf{q} = \mathbf{k}_{\text{out}} - \mathbf{k}_{\text{in}}$. Its three Cartesian components are given by $q_x = k \cos(\beta) \sin(2\theta)$, $q_y = k[\cos(\beta) \cos(2\theta) - \cos(\alpha)]$, and $q_z = k[\sin(\alpha) + \sin(\beta)]$, where $k = 2\pi/\lambda$. For

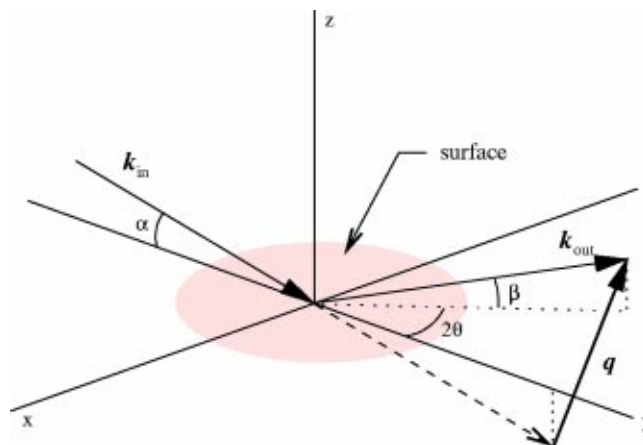


FIG. 1. X-ray scattering geometry.

all the x-ray data reported here, scattered intensities were measured using a NaI scintillation detector. Two sets of crossed Huber slits were placed between the sample and the detector, one set located at $S_1 = 183$ mm and the other (detector slits) at $S_2 = 657$ mm from the sample center. In what follows, the height and width of slit opening at S_i are denoted as (H_i, W_i) .

1. Specular reflectivity and off-specular diffuse scattering

In XR, intensity I reflected from the surface at the specular condition ($\beta = \alpha, 2\theta = 0; q_{xy} = 0$) is measured as a function of the incident angle α or wave vector transfer $q_z = 2k \sin(\alpha)$ along the surface normal. The reported signal is the difference between the intensity measured at the specular position ($2\theta = 0$) and the background intensity that was measured at 2θ offsets of $\pm 2\theta_b = \pm 0.25^\circ$. The opening of the detector slits at S_2 was set to $(H_2, W_2) = (2.5 \text{ mm}, 3.0 \text{ mm})$ and corresponded to angular detector resolutions of $\delta\beta = 0.22^\circ$ and $\delta(2\theta) = 0.26^\circ$, or equivalently, reciprocal-space resolutions of $\delta q_x = 0.0185 \text{ \AA}^{-1}$, $\delta q_y = 0.0019 q_z$, and $\delta q_z = 0.0155 \text{ \AA}^{-1}$.

XOSDS was measured using a β -scan method, in which the incident angle α is fixed and intensities scattered in the incidence plane ($2\theta = 0$) are measured as a function of the output angle β . The background intensities were measured at 2θ offsets of $2\theta_b = \pm 0.3^\circ$ and subtracted from the signal at $2\theta = 0$. The detector slit setting of $(H_2, W_2) = (1.0 \text{ mm}, 3.0 \text{ mm})$ used for the β scans corresponded to angular resolutions of $\delta\beta = 0.087^\circ$ and $\delta(2\theta) = 0.26^\circ$. The equivalent q -space resolutions are given by $\delta q_x = 0.0185 \text{ \AA}^{-1}$ and $\delta q_z = 0.0062 \text{ \AA}^{-1}$, while the q_y resolution varied with β as $\delta q_y = k \sin(\beta) \delta\beta = (0.0062 \text{ \AA}^{-1}) \times \sin(\beta)$.

The measured quantity for XOSDS is the normalized intensity difference $\Delta I(\alpha, \beta)/I_0$, where I_0 is the incident intensity and

$$\Delta I(\alpha, \beta) = I(\alpha, \beta, 2\theta = 0) - \left(\frac{1}{2}\right)[I(\alpha, \beta, +2\theta_b) + I(\alpha, \beta, -2\theta_b)]. \quad (1)$$

The specular reflectivity $R(q_z)$ measured in XR is a special case of the above, i.e., $R(\alpha) = \Delta I(\alpha, \beta = \alpha)/I_0$. In general,

the observed intensity is equal to the convolution of the differential cross section $d\sigma/d\Omega$ with an instrumental resolution function Ξ . For the experimental setups described above, the size of the detector slit opening is much larger than the cross sectional area A_0 of the incident beam (0.1×0.5 mm). Therefore it is appropriate to take $\Xi=1$ inside the resolution volume and $\Xi=0$ outside, such that

$$\frac{I(\alpha, \beta, 2\theta)}{I_0} = \int_{\beta_-}^{\beta_+} d\beta' \int_{2\theta_-}^{2\theta_+} d(2\theta') \frac{1}{A_0} \frac{d\sigma}{d\Omega}(\alpha, \beta', 2\theta'), \quad (2)$$

where $\beta_{\pm} = \beta \pm \delta\beta/2$ and $2\theta_{\pm} = 2\theta \pm \delta(2\theta)/2$. An equivalent expression based on the integration in the reciprocal space can be obtained by using the approximation $d\Omega \approx d\beta d(2\theta) \approx d^2\mathbf{q}_{xy} / [k^2 \sin(\beta)]$.

In the case of liquid surfaces, the scattering cross section is characterized by a power-law behavior of form $d\sigma/d\Omega \sim 1/q_{xy}^{2-\eta}$, where $0 < \eta = (k_B T / 2\pi\gamma) q_z^2 < 2$.^{68,69} This behavior originates from the two-dimensional nature of the interface and the presence of capillary waves, which are thermally excited fluctuations of liquid/gas interfacial heights $h(r_{xy})$ against surface tension γ . If the liquid surface is laterally homogeneous and height fluctuations of all interfaces are conformal with each other, $d\sigma/d\Omega$ is described well by the following normalized form:⁷⁰⁻⁷²

$$\frac{1}{A_0} \left(\frac{d\sigma}{d\Omega} \right)_{hmg} \approx \frac{1}{16\pi^2} \left(\frac{q_c}{2} \right)^4 \frac{|\Phi_0(q_z)|^2}{q_z^2 \sin(\alpha)} \frac{2\pi\eta}{q_{xy}^2} \left(\frac{q_{xy}}{q_{max}} \right)^\eta, \quad (3)$$

where $q_c = 2k \sin(\alpha_c)$ is the critical wave vector for total reflection (for water subphase, $q_c = 0.0218 \text{ \AA}^{-1}$ or $\alpha_c = 0.154^\circ$ at $\lambda = 1.55 \text{ \AA}$). The inverse $2\pi/q_{max}$ of the upper cutoff wave vector corresponds to the smallest capillary wavelength, which is on the order of the nearest-neighbor distance between molecules on the surface. The structure factor $|\Phi_0(q_z)|^2$ arises from an average local or ‘‘intrinsic’’ electron density profile $\langle \rho_{T=0}(z) \rangle$ across the interface and can be expressed as⁷³

$$|\Phi_0(q_z)|^2 = \frac{R_{T=0}(q_z)}{R_F(q_z)}, \quad (4)$$

where $R_F(q_z)$ is the Fresnel reflectivity of an ideally flat and sharp subphase/gas interface. $R_{T=0}(q_z)$ refers to the reflectivity due to the intrinsic profile $\langle \rho_{T=0}(z) \rangle$ that would be obtained if the capillary waves were absent, i.e., if $\langle h^2(0) \rangle = 0$. In the limit $q_z \gg q_c$, Eq. (4) approaches the well-known expression based on the Born approximation⁷⁰⁻⁷²

$$|\Phi_0(q_z)|^2 \approx \left| \int_{-\infty}^{+\infty} dz \frac{d}{dz} \left[\frac{\langle \rho_{T=0}(z) \rangle}{\rho_\infty} \right] e^{-iq_z z} \right|^2, \quad (5)$$

where ρ_∞ is the electron density in the bulk subphase ($\rho_\infty = 0.334 \text{ e/\AA}^3$ for water). For small values of q_z that are comparable to q_c , Eq. (4) can be evaluated by using the matrix method of the Parratt formalism, which is based on a division of $\langle \rho_{T=0}(z) \rangle$ into many constant-density slabs and the application of the exact boundary conditions at each slab/slab interface.^{74,75}

In the analysis, the intrinsic profile $\langle \rho_{T=0}(z) \rangle$ is extracted by constructing a model profile and fitting the corre-

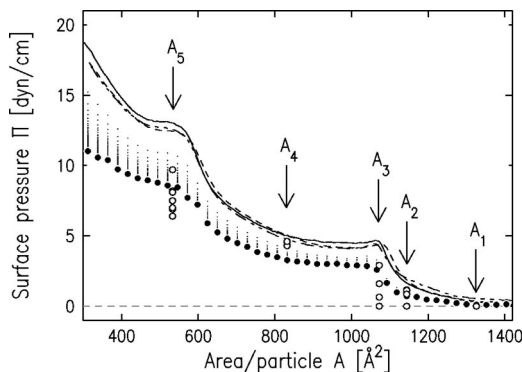


FIG. 2. Stepwise continuous (lines) and relaxation (filled circles) isotherms on AuSHDA films on HCl/water subphase ($pH=3$) at 25°C . Points where x-ray measurements were made are indicated by open circles and A_i , where $A_1=1325 \text{ \AA}^2/\text{particle}$, $A_2=1145 \text{ \AA}^2/\text{particle}$, $A_3=1070 \text{ \AA}^2/\text{particle}$, $A_4=830 \text{ \AA}^2/\text{particle}$, and $A_5=535 \text{ \AA}^2/\text{particle}$.

sponding $R(q_z)$ based on Eqs. (1)–(5) to the measured XR data. This procedure also allows the extraction of the structure factor $|\Phi_0(q_z)|^2$. Assuming that this factor is known, the theoretical XOSDS curve $[\Delta I(\alpha, \beta)/I_0]_{hmg}$ that would be expected for a homogeneous film can be calculated with no adjustable parameters and can be compared with the observed intensity $\Delta I(\alpha, \beta)/I_0$. If there exist some thermal or static surface inhomogeneities (i.e., lateral density fluctuations other than those due to capillary waves) at lateral length scales that are accessible by β scans ($100 \text{ \AA} - 1 \mu\text{m}$), then, excess scattering $\Delta I/I_0 - [\Delta I/I_0]_{hmg} > 0$ will be observed in off-specular regions.^{70,76}

2. Grazing incidence diffraction

All the GID measurements to be reported, including the characterization of Bragg rods,⁷⁷ were made by scanning the intensities scattered away from the incidence plane ($2\theta \neq 0$) and near the surface plane ($0 < \beta < 5^\circ$), as a function of 2θ or the lateral wave vector q_{xy} . The incident angle was fixed at $\alpha = 0.12^\circ$ ($< \alpha_c = 0.154^\circ$), corresponding to an illuminated footprint of extension ~ 50 mm along the incident beam direction. The slit settings used in typical scans were: $(H_1, W_1) = (8.0 \text{ mm}, 2.0 \text{ mm})$ at S_1 and $(H_2, W_2) = (11.5 \text{ mm}, 2.0 \text{ mm})$ at S_2 . The in-plane resolution was limited by the horizontal slit width W_1 at S_1 and corresponded to a FWHM (full width at half maximum) resolution of $\delta(2\theta) = W_1 / (S_2 - S_1) = 0.24^\circ$ or $\delta q_{xy} \approx 2k \delta(2\theta) = 0.017 \text{ \AA}^{-1}$. Due to the relatively large vertical opening H_2 of the detector slits, signals scattered over $\Delta\beta = 1.0^\circ$ or $\Delta q_z = 0.071 \text{ \AA}^{-1}$ were accepted by the detector.

III. RESULTS AND DISCUSSION

A. Π - A isotherms

Representative isotherms obtained from AuSHDA films at 25.0°C are shown in Fig. 2. Three separate stepwise continuous scans (lines; each from a fresh film) are plotted together to demonstrate the reproducibility of the isotherm. A relaxation isotherm is indicated by the filled circles. The only significant difference between the two types of isotherms is that at a given area/particle A , the surface pressure in the

relaxation isotherm is consistently lower than that in the continuous isotherm. Apart from this difference due to relaxation effects, the qualitative shape of the isotherms is nearly independent of the two different compression methods used, and the main features in the isotherms occur at almost the same values of A .

The isotherms are characterized by the appearance of a broad plateaulike region of finite surface pressure ($\Pi \sim 5$ dyne/cm in the continuous scans) whose width is consistent with a first-order monolayer/bilayer transition. At $A \sim 1100 \text{ \AA}^2/\text{particle}$ (between A_2 and A_3 in Fig. 2), just to the right of this plateau where an initial steep rise in Π is observed, the entire surface should be coated uniformly by a close-packed AuSHDA monolayer. At $A \sim A_3 = 1070 \text{ \AA}^2/\text{particle}$, the increase in Π is halted and replaced by the plateau, indicating a collapse of the monolayer and the beginning of a transfer of particles into the third dimension in some way. Compression across the plateau region leads to only a very slow increase in Π until a second well-defined rise is observed around $A \sim 600 \text{ \AA}^2/\text{particle}$. The fact that the area/particle values over this second rise are close to half of the values observed for the initial rise on the low-density side of the plateau suggests that the AuSHDA film consists primarily of a bilayer at $A \sim 600 \text{ \AA}^2/\text{particle}$. According to this interpretation, the plateau region corresponds to coexistence between monolayer and bilayer domains, with the bilayer fraction increasing with compression. Other Langmuir films that undergo a monolayer/bilayer transition, such as those of rodlike polypeptide PBLG,⁷⁶ are characterized by very similarly shaped isotherms.

Figure 2 shows some quantitative differences between the two types of isotherms. At large area ($A > 1150 \text{ \AA}^2/\text{particle}$), the continuous scans show a gradual increase in Π (from $\Pi \sim 0$), but the surface pressure drops nearly to zero if the film is allowed to relax sufficiently. This is probably due to incomplete surface coverage at large area and solidlike stiffness of AuSHDA monolayer islands, between which bare or uncoated surface areas still remain. As expected, the difference in Π between the two isotherms grows with compression across and past the first plateau, indicating close packing of particles over these high-density regimes. Although the continuous scans display another steep rise in Π below $A \sim 450 \text{ \AA}^2/\text{particle}$, such a feature is absent in the relaxation isotherm, which only shows a gradual Π increase over the same region. This seems to indicate that the layer-by-layer growth of the film with compression does not continue beyond the bilayer, but either multilayer domains or bulk aggregates are being formed at the highest densities shown in Fig. 2.

As indicated by open circles in Fig. 2, x-ray measurements were made on films at $A = A_1$ through A_5 , where $A_1 = 1325$, $A_2 = 1145$, $A_3 = 1070$, $A_4 = 830$, and $A_5 = 535 \text{ \AA}^2/\text{particle}$. The XR results to be discussed below provide strong evidence that the AuSHDA film indeed undergoes a compression-induced monolayer/bilayer transition.

B. XR: Structures along surface normal

Representative reflectivity data obtained from AuSHDA films are plotted in terms of the normalized reflectivity R/R_F

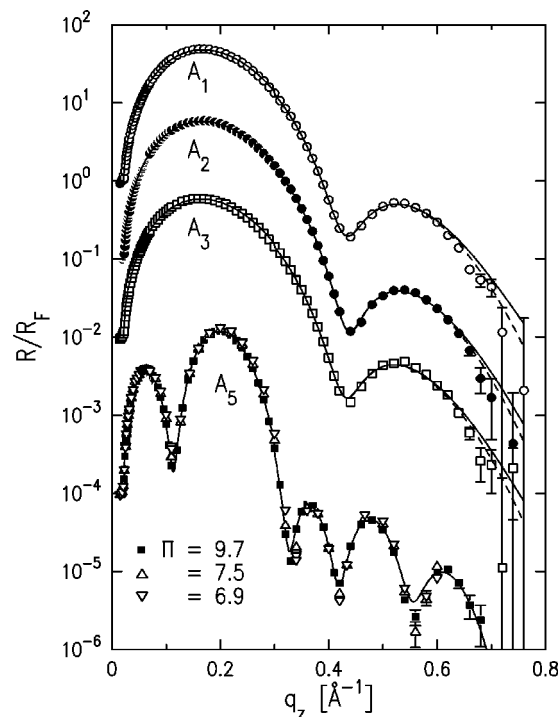


FIG. 3. Specular reflectivity data (symbols) normalized to the Fresnel reflectivity, measured from AuSHDA films at points A_1 , A_2 , A_3 , and A_5 in the isotherm. The three sets of data taken at A_5 ($\Pi = 9.7, 7.5,$ and 6.9 dyne/cm) are plotted together. The data taken at different A are shifted vertically for clarity. The lines are the best-fit R/R_F curves based on box-model average intrinsic profiles $(\rho_{T=0}(z))/\rho_\infty$. For A_1 , A_2 , and A_3 , the solid line and the dashed line are from type I and type II profiles, respectively.

in Fig. 3. The top three curves showing a nearly identical oscillation behavior correspond to monolayers at $A = A_1$, A_2 , and A_3 . The q_z positions of two maxima and a minimum evident in each R/R_F curve shift very little between these data sets, indicating that the films at these surface densities have roughly the same thickness. The amplitude of the oscillation is very large; for example, $R/R_F \sim 60$ at $q_z = 0.16 \text{ \AA}^{-1}$ for the first maximum in the data for the film at A_3 . This indicates the presence of a surface layer with much higher density than that in the bulk subphase, as expected for AuSHDA films. Although it is difficult to see from the figure, the amplitude for the first maximum at area A_1 ($R/R_F \sim 48$ at $q_z = 0.17 \text{ \AA}^{-1}$) is smaller than for A_3 . This indicates that the average layer density at A_1 is lower than at A_3 and probably originates from incomplete surface coverage at large area. The data obtained from the other side of the coexistence plateau at A_5 , where the film is expected to be a bilayer, are shown on the bottom of Fig. 3. For this area, three separate data sets obtained at $\Pi = 9.7, 7.5,$ and 6.9 dyne/cm are plotted on top of each other. The reproducibility of the data evidenced by a good overlap between them demonstrates that the average film structure along the surface normal is stable over this range of Π . It is clear from the much faster oscillation of these R/R_F curves that the film at A_5 must be significantly thicker than the monolayers at A_1 , A_2 , and A_3 .

The quantitative analysis of the R/R_F data has been carried out by using “box models” for the average intrinsic

profile $\langle \rho_{T=0}(z) \rangle$, in which each layer is represented by a box of thickness l_i and relative density $\phi_i = \rho_i / \rho_\infty$. The interfacial diffuseness of the profile (or short-range intrinsic roughness of noncapillary origin) between adjacent boxes i and $j = i + 1$ is described by an error function, whose gradient is a Gaussian with standard deviation $\sigma_{P,ij}$. Theoretical R/R_F curves based on Eqs. (1)–(5), with the intrinsic structure factor $|\Phi_0(q_z)|^2$ given by box-model profiles $\langle \rho_{T=0}(z) \rangle$, were fitted to the observed data by using the known values of T , $\gamma = \gamma_w - \Pi$ ($\gamma_w = 72$ dyne/cm for water at 25 °C), and the detector resolutions. The upper cutoff wave vector in Eq. (3) was fixed at $q_{\max} = 0.2 \text{ \AA}^{-1}$, which corresponds to the position of the lowest-order GID peak observed from AuSHDA films (to be discussed later). This assignment of q_{\max} is equivalent to setting the shortest capillary wavelength to the size of AuSHDA particles. Any capillary modes with even shorter wavelengths, if they are not completely quenched, are assumed to contribute to the profile roughness $\sigma_{P,ij}$ in $\langle \rho_{T=0}(z) \rangle$. The separation of their contribution from the true intrinsic roughness would require temperature-dependent measurements.^{71,78,79}

As will be shown below, the average electron density within the AuSHDA film relative to that of water can be as high as $\phi \sim 5.6$. This implies that in the range $q_c = 0.0218 \text{ \AA}^{-1} < q_z < \sqrt{\phi} q_c \sim 0.05 \text{ \AA}^{-1}$, the electric fields within the layer are evanescent waves and the penetration of x rays into the bulk subphase occurs only through tunneling across this layer. In such cases, the applicability of the Born approximation (BA) requires that $q_z \gg \sqrt{\phi} q_c$.⁷³ Therefore, for the fitting over the low q_z range $0.06 < q_z < 0.3 \text{ \AA}^{-1}$, the factor $|\Phi_0(q_z)|^2$ was evaluated by employing the Parratt formalism, where the box-model intrinsic profile $\langle \rho_{T=0}(z) \rangle$ was divided into many slabs of thickness 0.1 \AA . For $q_z > 0.3 \text{ \AA}^{-1}$, the calculation of the fitting curve was switched to the one based on the BA expression Eq. (5) for $|\Phi_0(q_z)|^2$. The fitting over these two q_z ranges were done simultaneously, using exactly the same density profile $\langle \rho_{T=0}(z) \rangle$.

The best fits to the R/R_F data are indicated by the lines (both solid and dashed ones) in Fig. 3, and the corresponding intrinsic profiles $\langle \rho_{T=0}(z) \rangle$ are illustrated in Fig. 4. The best-fit values for the box-model parameters are summarized in Table I.

For the monolayers at $A = A_1, A_2$, and A_3 , the use of a single box in the model profile is sufficient to obtain good fits. However, for each set of R/R_F data, the analysis produced two sets of parameters that fit the data equally well. For one set of parameters (type I), the intrinsic diffuseness parameter $\sigma_{P,1g}$ for the layer/gas interface is larger than $\sigma_{P,w1}$ for the water/layer interface ($\sigma_{P,1g} > \sigma_{P,w1}$); for the other set (type II), the opposite holds ($\sigma_{P,1g} < \sigma_{P,w1}$). In Fig. 3, the fits based on types I and II are indicated by the solid and dashed curves, respectively. Figure 4(a) compares the type-I and type-II intrinsic profiles for the AuSHDA monolayer at $A = A_3$. From the obtained data, it is not possible to determine which of the two best-fit profiles better represents the actual profile. This ambiguity probably arises from a combination of the limited q_z range of the data and the absence of phase information in the complex number $\Phi_0(q_z)$, as discussed previously by Pershan.⁸⁰ This question about the

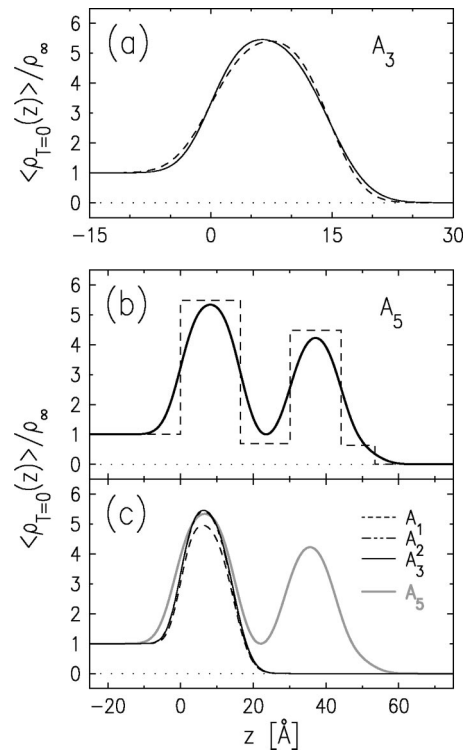


FIG. 4. Average intrinsic electron-density profiles $\langle \rho_{T=0}(z) \rangle / \rho_\infty$ extracted from the best fits to the R/R_F data. (a) AuSHDA monolayer at A_3 , where the solid line is for type-I profile and the dashed one is for type-II profile. (b) AuSHDA bilayer at A_5 , where the dashed lines are from the four-box model. Panel (c) compares the profiles obtained at different A .

uniqueness of extracted density profiles cannot be resolved here. However, Fig. 4(a) shows only slight differences in shape between the type-I and type-II profiles, and the two profiles are characterized by a single layer of similar density and thickness (also see Table I).

The intrinsic profiles $\langle \rho_{T=0}(z) \rangle$ obtained from the monolayer at A_3 , where the surface coverage should be complete, can be used to estimate the typical size of the Au cores. At $A = A_3$, the thickness and density parameters of the single box layer are given by $l_1 \sim 14.5 \text{ \AA}$ and $\phi_1 \sim 5.6$. These two parameters provide two independent measures of the mean Au-core diameter D . First, approximating the Au core as a uniform sphere of diameter D , the FWHM $\Delta z = D/\sqrt{2}$ of the density distribution given by the projection of the sphere onto the z axis can be identified with the thickness l_1 to obtain $D_1 = \sqrt{2} \Delta z = \sqrt{2} l_1 = 20.5 \text{ \AA}$. Second, the electron density within the Au core is $\phi_{\text{Au}} = \rho_{\text{Au}} / \rho_\infty = 13.3$ (bulk values: $\rho_{\text{Au}} = 4.46 \text{ e/\AA}^3$ for fcc gold crystal; $\rho_\infty = 0.334 \text{ e/\AA}^3$ for water), whereas the density for the alkyl chains around each core is roughly on the order of $\phi_{\text{alk}} = 1$ (assuming close packing). According to these numbers and the assumption $\phi_1 = F \cdot \phi_{\text{Au}} + (1 - F) \cdot \phi_{\text{alk}}$, a fraction $F \sim 0.37$ of the surface area can be attributed to the Au cores in the plane through their centers. As will be shown in Sec. III D, the observed GID patterns indicate that the AuSHDA particles form hexagonally packed 2D domains of nearest-neighbor distance $a = 34 \text{ \AA}$. Taking $A_{\text{hex}} = (\sqrt{3}/2)a^2 = 1000 \text{ \AA}^2/\text{particle}$ as a measure of the average area/particle at close packing, the average Au core diameter based on ϕ_1 is equal to D_ϕ

TABLE I. Best-fit parameters for the average local electron-density profile $\langle\rho_{T=0}(z)\rangle/\rho_\infty$ across the water/AuSHDA/gas interface.

One-box model for AuSHDA monolayers.										
A [Å ² /part.]	Π [dyne/cm]	Type ^a	$\phi_1 = \rho_1/\rho_\infty$	l_1 [Å]	$\sigma_{P,w1}$ [Å]	$\sigma_{P,lg}$ [Å]				
1325	0	I	5.09±0.12	14.44±0.15	2.79±0.14	3.85±0.18				
		II	5.02±0.12	14.59±0.16	3.47±0.19	3.13±0.12				
1145	0.3	I	5.63±0.13	14.31±0.15	3.08±0.14	3.90±0.18				
		II	5.57±0.13	14.41±0.15	3.59±0.19	3.37±0.12				
1070	2.9	I	5.65±0.15	14.49±0.17	3.02±0.16	3.95±0.19				
		II	5.58±0.15	14.61±0.19	3.63±0.22	3.31±0.14				
Four-box model for a AuSHDA bilayer. ^b										
A [Å ² /part.]	Π [dyne/cm]	ϕ_1	ϕ_2	ϕ_3	ϕ_4	l_1 [Å]	l_2 [Å]	l_3 [Å]	l_4 [Å]	σ_P [Å]
535	9.7	5.49 ±0.11	0.69 ±0.12	4.49 ±0.13	0.63 ±0.13	16.44 ±0.27	13.73 ±0.28	13.97 ±0.31	9.37 ±0.82	3.83 ±0.15

^aType I: $\sigma_{P,w1} < \sigma_{P,lg}$; type II: $\sigma_{P,w1} > \sigma_{P,lg}$.

^bSingle parameter σ_P was used for profile diffuseness at each box interface.

$=2(F \cdot A_{\text{hex}}/\pi)^{1/2} = 22 \text{ \AA}$. The good agreement between the two independently determined diameters D_l and D_ϕ suggests that they reflect the typical Au core size of the AuSHDA particles. Moreover, it shows that the intrinsic profiles $\langle\rho_{T=0}(z)\rangle$ obtained at A_1 , A_2 , and A_3 are consistent with monolayers of AuSHDA particles.

The formation of a bilayer on the high-density side of the coexistence plateau is clearly demonstrated by the intrinsic profile $\langle\rho_{T=0}(z)\rangle$ obtained at A_5 , shown in Fig. 4(b). The fitting of the R/R_F data at A_5 required the use of a four-box model to construct the nonuniform bilayer profile, but in order to minimize the number of fitting parameters, a single parameter σ_P was used to describe the profile diffuseness of all the box/box interfaces. The four-box parameters for this bilayer are listed in Table I, and the corresponding boxes in the model are indicated by the dashed line in Fig. 4(b). The same bilayer profile is compared with the type-I profiles of the monolayers at A_1 , A_2 , and A_3 in Fig. 4(c).

The presence of two distinguishable layers in the bilayer is evident from the two well-separated maxima in the profile in Fig. 4(b), indicating that the AuSHDA particles belong to only one or the other of the layers. Based on the positions of the two peaks, the central planes of the two layers are separated by a distance of $l_{12} = 29.0 \text{ \AA}$ along the surface normal. The fact that the relative density is close to unity ($\langle\rho_{T=0}\rangle/\rho_\infty \sim 1$) at the minimum between the layers is consistent with the presence of alkyl chains in this interlayer region and the exclusion of Au cores. Figure 4(c) shows that the first layer of the bilayer, right above the subphase, is slightly thicker than the monolayers are but its peak density is comparable to that of the monolayer at A_3 . The second layer closer to the gas above is, on average, less dense (by $\sim 18\%$) than the first layer, indicating that this layer on top is the one newly created by lateral compression.

Collectively, these observations can be interpreted as follows: The AuSHDA monolayer achieves a maximum lateral density sustainable at the low-density end of the coexistence plateau (at A_3). Subsequent compression across the plateau displaces more and more AuSHDA particles out of the monolayer up onto the second layer to form a bilayer. It

appears that during this process, a point is reached where the occupied fraction of the second layer becomes large enough to hinder a further upward transfer of AuSHDA particles and the first layer begins to experience the effect of lateral compression. This can be seen from the fact that the first layer of the bilayer is thicker than the monolayer and also from the gradual increase in Π for $A < \sim 800 \text{ \AA}^2/\text{particle}$ (see Fig. 2). These observations suggest that compression across the plateau increases the width of the distribution in the vertical positions of AuSHDA particles in the first layer. On the basis of this and the less than full coverage of the second layer in the bilayer, it seems reasonable to suppose that the bilayer is less likely to be laterally homogeneous than the monolayer. The surface homogeneity of AuSHDA films is considered in the following section.

C. XOSDS: Surface homogeneity

The results of β scans measured with the incident angle fixed at $\alpha = 1.0^\circ$ and 2.0° are summarized in Fig. 5 for an

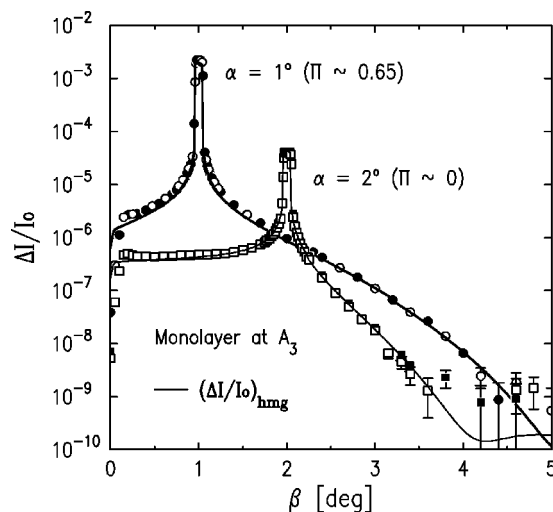


FIG. 5. β scans at $\alpha = 1^\circ$ (circles; $\Pi \sim 0.65$ dyne/cm) and $\alpha = 2^\circ$ (squares; $\Pi \sim 0.0$ dyne/cm) from the AuSHDA monolayer at A_3 . The solid lines are the theoretical curves expected for a homogeneous film.

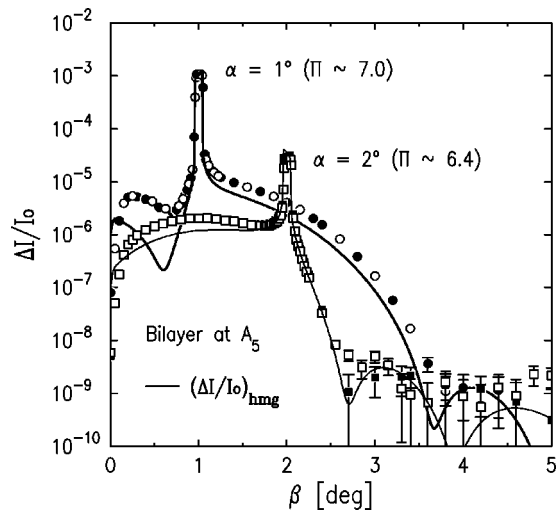


FIG. 6. β scans at $\alpha=1^\circ$ (circles; $\Pi\sim 7.0$ dyne/cm) and $\alpha=2^\circ$ (squares; $\Pi\sim 6.4$ dyne/cm) from the AuSHDA bilayer at A_5 . The solid lines are the theoretical curves expected for a homogeneous film.

AuSHDA monolayer at A_3 and in Fig. 6 for a bilayer at A_5 . For each scan, a large peak at $\beta=\alpha$ corresponds to the specular reflection. The surface enhancement peak (“Yoneda” peak), which is expected to occur at $\beta=\alpha_c$ ($\sim 0.154^\circ$), is not very visible in these scans; this is a consequence of the fact that this peak tends to be suppressed by the presence of a high-density layer on the surface.⁷³ The characterization of off-specular spectra has been limited by the resolution $\delta\beta$ near the specular peak and by low counting rates at large β ($\sim 5^\circ$). In terms of the lateral wave vector transfer q_y , these limits correspond to a range given by: $k \sin(\alpha)\delta\beta=1.1\times 10^{-4} \text{ \AA}^{-1} < |q_y| < 1.5\times 10^{-2} \text{ \AA}^{-1}$ for $\alpha=1.0^\circ$ and $2.2\times 10^{-4} \text{ \AA}^{-1} < |q_y| < 1.3\times 10^{-2} \text{ \AA}^{-1}$ for $\alpha=2.0^\circ$. Therefore the lateral density fluctuations being probed by these measurements are only those with length scales in the range of $\sim 100 \text{ \AA} - 1 \mu\text{m}$.

In Figs. 5 and 6, the solid curves represent the theoretical normalized intensity difference $[\Delta I(\alpha,\beta)/I_0]_{hmg}$ expected from the presence of capillary waves and the assumption that the given film is otherwise laterally homogeneous. For each film, the intrinsic structure factor $|\Phi_0(q_z)|^2$ used in the calculation is based on the fitting of the specular reflectivity data that was obtained from the same film immediately before the β scans. All the other parameters needed for the calculation are known, except that $q_{max}=0.2 \text{ \AA}^{-1}$ has been assumed as in the case of XR.

Figure 5 shows that in the case of a monolayer at A_3 , the observed off-specular intensities $\Delta I(\alpha,\beta)/I_0$ agree fairly well with the expected curve $[\Delta I(\alpha,\beta)/I_0]_{hmg}$. This implies that the off-specular scattering can be attributed almost entirely to the interfacial height fluctuations due to capillary waves and that the close-packed AuSHDA monolayer at A_3 is laterally homogeneous. This result is analogous to the case of a homogeneous PBLG monolayer under a finite surface pressure.^{70,76}

By contrast, the β -scan data shown in Fig. 6 for a bilayer at A_5 are consistently higher than the homogeneous curve $[\Delta I(\alpha,\beta)/I_0]_{hmg}$ in the off-specular regions, except for the

range $\beta > \alpha = 2.0^\circ$ where both the data and the theory show low intensities. It can be shown that if the local density $\rho_{T=0}(\mathbf{r})$ deviates from its lateral average $\langle \rho_{T=0}(z) \rangle$, i.e., if $\delta\rho_{T=0}(\mathbf{r}) = \rho_{T=0}(\mathbf{r}) - \langle \rho_{T=0}(z) \rangle \neq 0$, then the scattering cross section acquires a *second term* beyond Eq. (3), which can be expressed as⁷⁶

$$\frac{1}{A_0} \left(\frac{d\sigma}{d\Omega} \right)_{inhmg} = \frac{1}{16\pi^2} \left(\frac{q_c}{2} \right)^4 \frac{1}{A_0} \left| \int d^3r e^{-i\mathbf{q}\cdot\mathbf{r}} e^{-iq_z h(r_{xy})} \frac{\delta\rho_{T=0}(\mathbf{r})}{\rho_\infty} \right|^2, \quad (6)$$

where the local interfacial height $h(r_{xy})$ fluctuates with capillary waves. Therefore the observation of *excess* off-specular scattering suggests that some form of lateral density inhomogeneities $\delta\rho_{T=0}(\mathbf{r}) \neq 0$ exist within the bilayer at A_5 . This result is similar to the case of a PBLG bilayer, for which the observation of excess off-specular scattering has been attributed to inhomogeneities in the newly formed second layer.^{70,76} The observation that the AuSHDA bilayer is less homogeneous than the monolayer is not too surprising given the high degree of compression that the film underwent prior to its formation and the incomplete coverage of the second layer, as pointed out at the end of the XR section.

Qualitatively, a close inspection of all curves in Fig. 6 shows that the magnitude $\Delta I(\alpha,\beta)/I_0 - [\Delta I(\alpha,\beta)/I_0]_{hmg} > 0$ of the excess scattering seems to decrease with increasing $q_z \sim k(\alpha + \beta)$. This behavior may be an indication that the laterally inhomogeneous regions are restricted to a certain thickness within the bilayer. Another possibility is the presence of long-wavelength height fluctuations (probably static) of AuSHDA particles that are not conformal with capillary fluctuations.

Another important observation from Fig. 6 is that although the theoretical curve $[\Delta I(\alpha,\beta)/I_0]_{hmg}$ for $\alpha=1.0^\circ$ oscillates with β and has a well-defined minimum at $\beta \sim 0.6^\circ$ or equivalently, at $q_y=4.0\times 10^{-4} \text{ \AA}^{-1}$ and $q_z=0.11 \text{ \AA}^{-1}$, such a dip in intensity is much less apparent in the actual data. The minimum at $q_z=0.11 \text{ \AA}^{-1}$ arises from the factor $|\Phi_0(q_z)|^2$ and corresponds to the first minimum in the R/R_F data shown for the bilayer in Fig. 3. Note that the value $\pi/q_z=28 \text{ \AA}$ compares well with $l_1+l_2=30.2 \text{ \AA}$ and $l_2+l_3=27.7 \text{ \AA}$, while all the density differences across the box/box interfaces are roughly of the same order of magnitude [except for the box-4/gas interface; see Table I and Fig. 4(b)]. Therefore the minimum at $q_z=0.11 \text{ \AA}^{-1}$ arises from the condition that x-ray waves scattered off from the subphase/box-1 and box-1/box-2 interfaces interfere destructively with those from the box-2/box-3 and box-3/box-4 interfaces, respectively. In other words, this dip in intensity would appear in the off-specular data only if the height fluctuations of first-layer and second-layer AuSHDA particles were well correlated over a lateral distance that is comparable to or larger than $q_y^{-1} \sim 2500 \text{ \AA}$. The strong suppression of the minimum in the data therefore suggests reduction of such conformality between the two layers of the bilayer.⁸¹

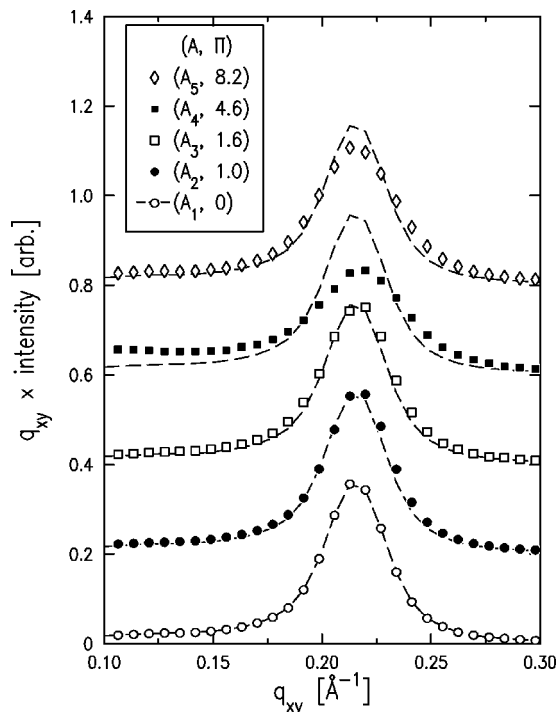


FIG. 7. A linear plot of the lowest-order GID peaks from AuSHDA films at various A and Π [dyne/cm], shifted vertically for clarity. The dashed lines are identical and correspond to the data from a monolayer at A_1 .

This inference is also consistent with a low degree of lateral homogeneity for the bilayer.

D. GID: In-plane structures

Representative GID patterns measured from AuSHDA films at various points in the isotherm are compared over a small range of q_{xy} in Fig. 7 (a linear plot) and over a larger range of q_{xy} in Fig. 8(a) (a semilog plot). In order to account for the fact that the length of the illuminated surface area that is viewed by the detector decreases with increasing q_{xy} as $\sim 1/q_{xy}$, the data is plotted as $q_{xy} \times \text{intensity}$. All the data shown in Figs. 7 and 8 were obtained from scans near the surface horizon ($0 < q_z < 0.074 \text{ \AA}^{-1}$). In Fig. 7, all the dashed lines are identical and correspond to the data from a monolayer at A_1 . Whether the film is a monolayer or a bilayer, the observed GID pattern is characterized by a strong peak at $q_{xy} = 0.215 \text{ \AA}^{-1}$. Since the peak is already present at A_1 , the in-plane structure associated with it must be spontaneously formed upon spreading of the film. The position of this peak is nearly independent of A or Π , and hence lateral compression appears to have very little effect upon the average inter-particle distance in the laterally ordered domains.

Figure 8(a) shows some evidence for the presence of additional higher-order peaks. The patterns contain a weak peak at $q_{xy} \sim 0.56 \text{ \AA}^{-1}$ and possibly another feature around $q_{xy} \sim 0.37 \text{ \AA}^{-1}$ that is even weaker. The positions of these weak higher-order peaks and the much more intense lowest-order peak at $q_{xy} = 0.215 \text{ \AA}^{-1}$ are all consistent with 2D hexagonal packing with a nearest-neighbor distance of $a = 34 \text{ \AA}$. The number of equivalent points in the corresponding hexagonal 2D reciprocal lattice is plotted as a function of

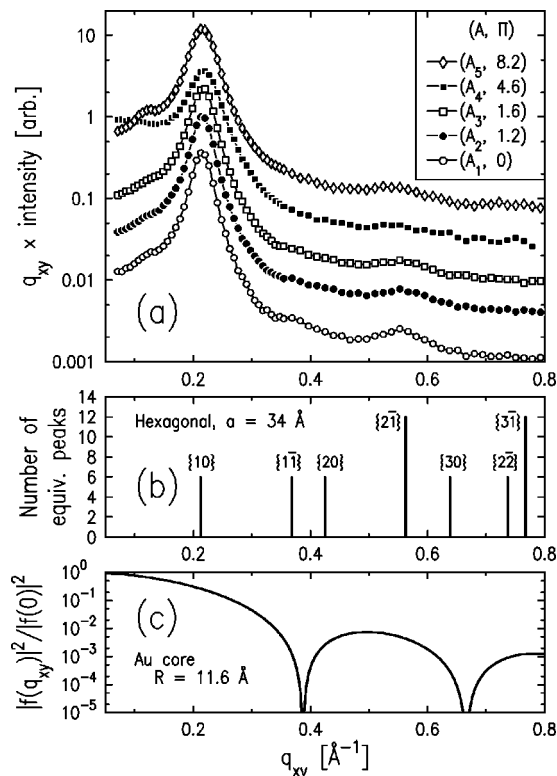


FIG. 8. (a) A semilog plot of GID data from AuSHDA films at various A and Π [dyne/cm], over larger q_{xy} range (shifted vertically for clarity), (b) the number of equivalent points in reciprocal space for a 2D hexagonal lattice with a nearest-neighbor distance $a = 34 \text{ \AA}$, and (c) calculated molecular form factor for a uniform sphere of diameter $D_{BR} = 23.2 \text{ \AA}$.

q_{xy} in Fig. 8(b), where the indices $\{hk\}$ are based on the primitive unit cell. Comparison between Figs. 8(a) and 8(b) shows that the three peaklike features in the data are located fairly close to the expected positions of the $\{10\}$, $\{1\bar{1}\}$, and $\{2\bar{1}\}$ peaks from the 2D hexagonal lattice.

In general, GID peaks are weaker and more difficult to observe at higher q_{xy} because the magnitudes of the molecular form factor and the Debye–Waller factor decrease with increasing q_{xy} . This is likely to be the reason for the absence of further higher-order peaks for $q_{xy} > 0.6 \text{ \AA}^{-1}$ in the observed GID patterns. The fact that the $\{2\bar{1}\}$ peak is discernable in the data probably arises from the relatively large number of reciprocal-lattice points at this value of q_{xy} [see Fig. 8(b)]. On the other hand, the $\{1\bar{1}\}$ and $\{20\}$ peaks are much less clearly visible in the data, even though they occur at lower q_{xy} than the $\{2\bar{1}\}$ peak. This can be explained in terms of the molecular form factor $|f(q)|^2$ of AuSHDA particles, as follows. Most of the contribution to $|f(q)|^2$ comes from the Au cores because of their much higher electron density compared with that of alkyl thiol chains around them. It can be shown that if the size polydispersity of Au cores is neglected and the core is approximated as a uniform sphere of radius $R = D/2$, the form factor is given by

$$|f(q)|^2 = |f(0)|^2 \left| \frac{3}{q^3 R^3} [\sin(qR) - qR \cos(qR)] \right|^2, \quad (7)$$

where $q^2 = q_{xy}^2 + q_z^2$ and $f(0)$ is equal to the total number of

TABLE II. Observed position G_{10} and FWHM Δq_{xy} of the lowest-order GID peak based on fits to the form $q_{xy}J(q_{xy}) \propto [1 + (q_{xy} - G_{10})^2/\sigma^2]^{-\nu}$ (plus a linear and a constant background terms), where $\Delta q_{xy} = 2\sigma(2^{1/\nu} - 1)^{1/2}$. An associated lateral correlation length ξ is defined as $\xi = 2/[\Delta q_{xy} - \delta q_{xy}]$, where the FWHM of the q_{xy} resolution is given by $\delta q_{xy} = 0.017 \text{ \AA}^{-1}$.

A [$\text{\AA}^2/\text{part.}$]	II [dyne/cm]	ν	G_{10} [$\pm 0.001 \text{ \AA}^{-1}$]	Δq_{xy} [$\pm 0.002 \text{ \AA}^{-1}$]	ξ [\AA]
1325	0	1.4 ± 0.2	0.214	0.032	130 ± 14
1145	1.0	1.7 ± 0.2	0.215	0.036	104 ± 10
1070	1.6	1.9 ± 0.3	0.215	0.038	94 ± 8
830	4.6	11 ± 13	0.217	0.050	61 ± 4
535	8.2	1.7 ± 0.2	0.215	0.042	80 ± 6

electrons contained in an Au core of radius R . Figure 8(c) plots the ratio $|f(q=q_{xy}, q_z=0)|^2/|f(0)|^2$ for the case of $R = D_{\text{BR}}/2 = 11.6 \text{ \AA}$, where D_{BR} is the Au-core diameter extracted from the Bragg-rod measurements to be described below. It should be noted that the curve has a minimum around $q_{xy} \sim 0.4 \text{ \AA}^{-1}$. The polydispersity of Au cores should smear out this minimum. It is nevertheless clear from this plot that the form factor arising from typical sizes of AuSHDA particles should lead to a very low intensity over the range of q_{xy} where the $\{1\bar{1}\}$ and $\{20\}$ peaks are located.

Based on the above results, the following observations can be made. First, the area occupied by each AuSHDA particle in the hexagonally packed domains is equal to $A_{\text{hex}} = (\sqrt{3}/2)a^2 = 1000 \text{ \AA}^2/\text{particle}$. The fairly good agreement between the microscopic area A_{hex} and the isotherm area A_3 ($=1070 \text{ \AA}^2/\text{particle}$; see Fig. 2) is consistent with complete surface coverage by a monolayer of close packed AuSHDA particles at the onset of the coexistence plateau. Second, from the nearest-neighbor distance of $a = 34 \text{ \AA}$ and the mean Au-core diameter of $D \sim 22 \text{ \AA}$ (see Sec. II A), the edge-to-edge separation between adjacent Au cores in the close-packed domains can be estimated to be about $\delta = a - D \sim 12 \text{ \AA}$. This spacing is clearly smaller than the length ($\sim 20 \text{ \AA}$) of stretched-out alkythiol chains $[\text{HS}-(\text{CH}_2)_{15}-\text{COOH}]$ in the all-*trans* conformation. This suggests that the close packing of AuSHDA particles in the monolayer results in a high degree of interpenetration between thiol chains or bundles of chains⁶⁰ from adjacent Au cores and/or a highly deformed and compressed shape of thiol “shells” around the cores as compared to their colloidal states in solution.

The extent of lateral positional correlations associated with the in-plane order can be estimated from the observed width of the GID peaks. For this purpose, the FWHM width Δq_{xy} of the $\{10\}$ peak at $q_{xy} = G_{10}$ has been extracted by fitting it to a Lorentzian raised to a power of ν with constant and linear background terms, such that the intensity above the background is proportional to $[1 + (q_{xy} - G_{10})^2/\sigma^2]^{-\nu}$. The FWHM width $\Delta q_{xy} = 2\sigma(2^{1/\nu} - 1)^{1/2}$ based on this fitting procedure is listed in Table II. The table also lists a lateral correlation length ξ defined as $\xi = 2/[\Delta q_{xy} - \delta q_{xy}]$ (experimental resolution: $\delta q_{xy} = 0.017 \text{ \AA}^{-1}$). This definition of ξ is strictly valid only when both the resolution function and the line shape of a peak in the GID cross section are described by Lorentzians ($\nu = 1$), such that the observed peak corresponding to the convolution of the two also has a Lorentzian shape. Since this condition does not hold in the

present case, the listed values of ξ should only be viewed as estimates.

For the monolayers at A_1 , A_2 , and A_3 , the extracted correlation length ranges from $\xi \sim 90$ to 130 \AA , which is only a few times larger than the nearest-neighbor distance $a = 34 \text{ \AA}$. Therefore the 2D hexagonal packing of AuSHDA particles is only short-range order in the monolayer. It is interesting to note that the ratio $\xi/a \sim 3-4$ is comparable to the ratio $D/\Delta D \sim 3-5$ between the mean and standard deviation in the distributions of Au core diameters in typical AuSCn samples.⁵⁸ This observation seems to suggest that the limited extent of positional correlations between AuSHDA particles originates from the polydispersity in their sizes.^{3,18,34,50} The A-dependent behaviors of the widths of the $\{10\}$ peaks shown in Fig. 7 and ξ in Table II seem to indicate that compression of the monolayer from A_1 to A_3 leads to a slight reduction in the degree of lateral order. Another indication of this is provided by a slight drop in the $\{2\bar{1}\}$ peak intensity with compression from A_1 to A_3 .

Such a disordering effect of lateral compression is more clearly evident for the film at A_4 (a mid point along the coexistence plateau), for which the $\{10\}$ peak is both broader and less intense than it is for the monolayers (see Fig. 7 and Table II). Another important observation is that at A_4 the intensity scattered at low $q_{xy} < 0.2 \text{ \AA}^{-1}$ is higher than that of the monolayers [see Fig. 8(a)]. This suggests that some nearest-neighbor pairs of AuSHDA particles are separated by lateral distances that are larger than $a = 34 \text{ \AA}$. Given that the occupied fraction of the second layer should only be about a half or less on average at A_4 , the observation of enhanced diffuse scattering at low q_{xy} is consistent with the presence of AuSHDA particles in the second layer.

After the film is compressed further to form a bilayer at A_5 , the diffuse intensities at low q_{xy} drop back to the level close to that of the monolayers, which is consistent with a more complete coverage of the second layer. The fact that the $\{10\}$ peak becomes also more intense and sharper than it is at A_4 , suggests that due to their increased number some of the second-layer particles now display the same hexagonal packing order that exists in the monolayer. However, Fig. 7 shows that the peak intensity for the bilayer is still not as high as that of the monolayers. This seems to indicate that in spite of a nearly twofold increase in the number of particles per unit area in going from a monolayer to a bilayer, the number of those belonging to *ordered* domains does not in-

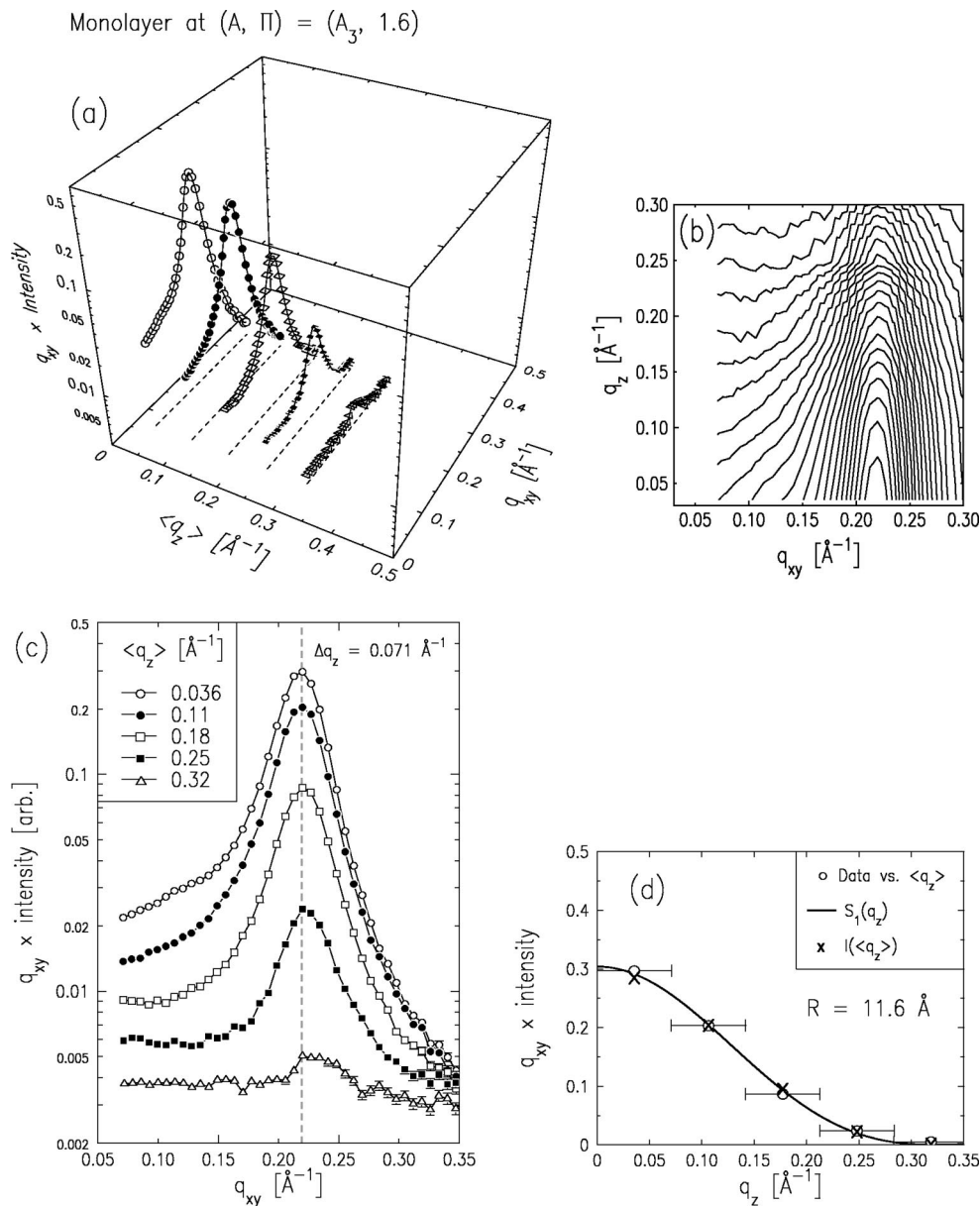


FIG. 9. Bragg-rod data from the AuSHDA monolayer at A_3 and $\Pi = 1.6$ dyne/cm. The 3D representation in (a) and the q_{xy} projection in (c) are semilog plots. The q_{xy} - q_z contour plot in (b) was generated from the data in (a), where the contours of constant intensity represent 25 equally spaced intervals between the maximum and the minimum in the logarithmically scaled intensity. The q_z projection in (d) is a linear plot. In (d), the data points (circles) correspond to the peak values in (c) and the horizontal bars represent the detector acceptance $\Delta q_z = 0.071 \text{\AA}^{-1}$. The scattering amplitude $S_1(q_z)$ (solid curve) and the integrated intensity $I(\langle q_z \rangle)$ (crosses) correspond to the best fit obtained by approximating the Au core with a uniform sphere of diameter $D_{BR} = 23.2 \text{\AA}$.

crease by the same amount. This issue is considered further below.

The q_z dependence of the intense $\{10\}$ peak has been characterized by taking a series of q_{xy} scans at different heights $\langle q_z \rangle$ above the surface. The results for the monolayer at A_3 are summarized in Fig. 9. The q_{xy} - q_z contour plot in Fig. 9(b) was generated from the data shown in Fig. 9(a), where the contours represent 25 equally spaced logarithmic intensity intervals between the maximum and the minimum. The plot of the data against q_{xy} in Fig. 9(c) shows that the center of the peak shifts very little with increasing $\langle q_z \rangle$, which is consistent with the behavior of a Bragg rod. The observed peak values (open circles) are plotted as a function of q_z in Fig. 9(d), where the horizontal bars represent the

fixed width $\Delta q_z = 0.071 \text{\AA}^{-1}$ of the detector opening. It is clear that the Bragg rod from the monolayer is centered at $q_z = 0$ and falls off monotonically with q_z . For a GID peak arising from a purely 2D structure, the scattering cross section depends on q_z only through the form factor (aside from the surface enhancement peak at $\beta = \alpha_c$, which is negligible in the present case). Therefore, for the monolayer, the scattering amplitude $S(q_z)$ along q_z should be described by the following form:

$$S_1(q_z) = S_0 \cdot |f(q_{xy} = G_{10}, q_z)|^2. \quad (8)$$

The intensity $I(\langle q_z \rangle)$ expected at $\langle q_z \rangle$ is given by the integration of $S(q_z)$ over $|q_z - \langle q_z \rangle| < \Delta q_z/2$. The theoretical intensity $I(\langle q_z \rangle)$ based on Eq. (8) and the form factor in Eq.

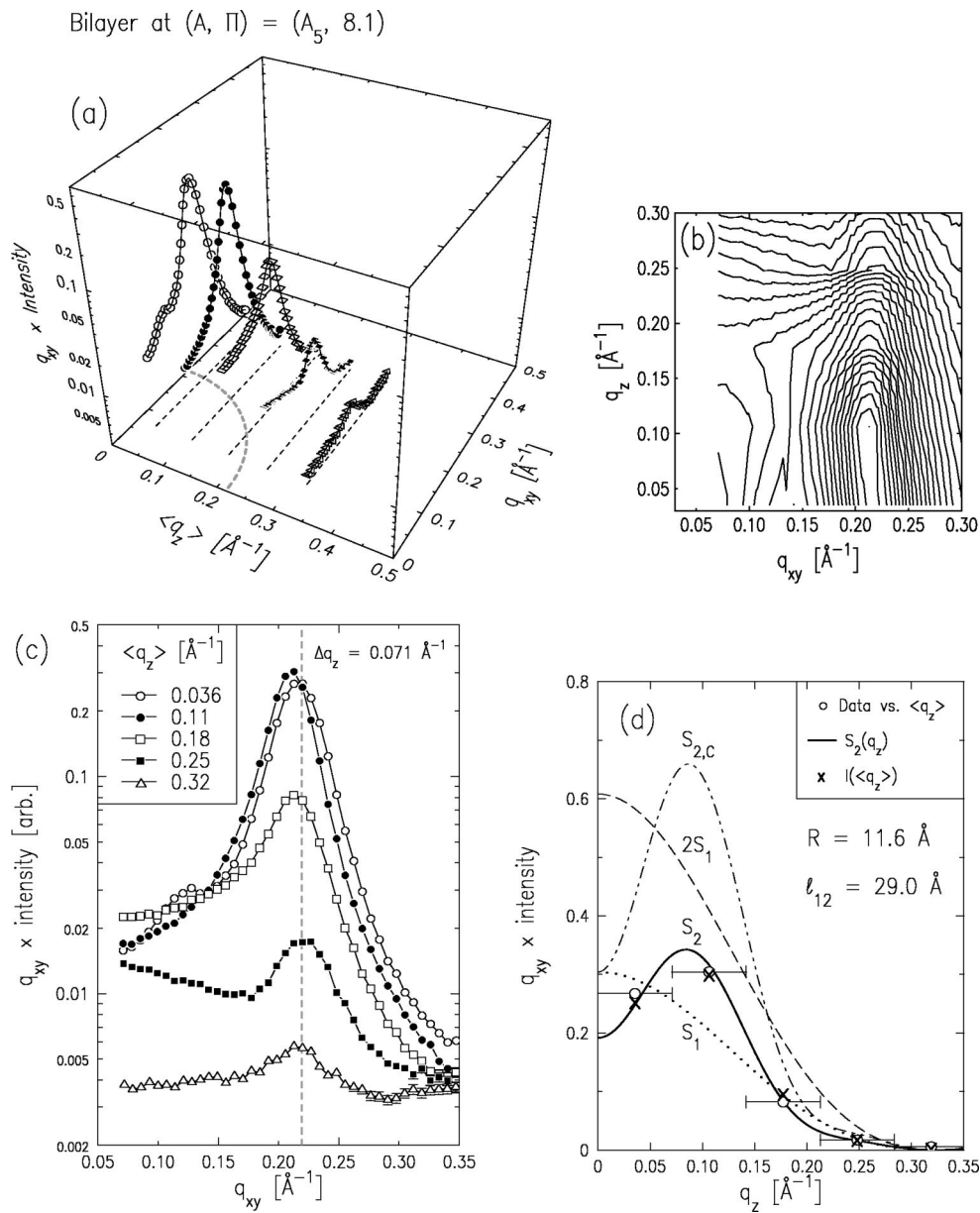


FIG. 10. Bragg-rod data from a AuSHDA bilayer at A_5 and $\Pi = 8.1$ dyne/cm. The 3D representation in (a) and the q_{xy} projection in (c) are semilog plots. The q_{xy} - q_z contour plot in (b) was generated from the data in (a), where the contours of constant intensity represent 25 equally spaced intervals between the maximum and the minimum in the logarithmically scaled intensity. The q_z projection in (d) is a linear plot. In (a), the dashed circle on the bottom describes $q = [q_{xy}^2 + q_z^2]^{1/2} = 0.216 \text{\AA}^{-1}$. In (d), the data points (circles) correspond to the peak values in (c) and the horizontal bars represent the detector acceptance $\Delta q_z = 0.071 \text{\AA}^{-1}$. See text for the details on the calculated scattering amplitudes S_i (curves) and the integrated intensity $I(\langle q_z \rangle)$ (crosses).

(7) has been fitted to the observed Bragg-rod data by varying the proportionality factor S_0 and the Au core radius R . The best fit is obtained at $R = 11.6 \pm 0.3 \text{\AA}$ or $D_{BR} = 23.2 \pm 0.6 \text{\AA}$, which is another independent measure of the mean Au core diameter D and corresponds well with the two other values $D_1 = 20.5 \text{\AA}$ and $D_\phi = 22 \text{\AA}$ determined earlier (see Sec. II A and III B). Figure 9(d) shows that the data agrees fairly well with the best-fit $I(\langle q_z \rangle)$ (crosses) and the corresponding $S_1(q_z)$ (solid curve). This agreement demonstrates that the observed peak indeed originates from a 2D structure of AuSHDA particles, i.e., from a monolayer.

The Bragg-rod data obtained from the bilayer at A_5 are shown in Fig. 10. Just as in the case of the monolayer, the $\{10\}$ peak remains well centered at $q_{xy} = G_{10}$ in the region

above the surface plane ($\langle q_z \rangle > 0$). However, diffuse scattering at low $q_{xy} < 0.2 \text{\AA}^{-1}$ shows a complicated behavior and is no longer characterized by a smooth decay with increasing q_z . In fact, a close inspection of Figs. 10(a)–10(c) suggests that in addition to the strong $\{10\}$ peak, there is enhanced diffuse scattering that could be consistent with a “ring” of radius $q = (q_{xy}^2 + q_z^2)^{1/2} \sim 0.2 \text{\AA}^{-1}$. This feature is suggestive of isotropic scattering and might be an indication for the presence of small 3D aggregates that are embedded in or sitting on top of the bilayer. It may also be due to some degree of interparticle correlations across the two layers of the bilayer.

Figure 10(d) shows the q_z dependence of the Bragg rod

that is based on the peak intensities of the q_{xy} scans in Fig. 10(c). In contrast to the case of the monolayer, the Bragg rod from the bilayer appears to display a maximum around $q_z \sim 0.1 \text{ \AA}^{-1}$. Also shown in the figure are several possible model curves for the scattering amplitude $S(q_z)$. The dotted curve $S(q_z) = S_1(q_z)$ is identical to the best-fit curve for the monolayer shown in Fig. 9(d). The bilayer would also exhibit this behavior, for example, if the in-plane order in the first layer remained the same as in the monolayer and the newly created second layer was completely disordered. The dashed curve $S(q_z) = 2S_1(q_z)$ in Fig. 10(d) describes the case in which each of the two layers exhibits the same degree of in-plane order as the monolayer but the layers are completely uncorrelated with each other. Finally, the curve $S(q_z) = S_{2,C}(q_z)$ describes a case of a perfectly correlated bilayer in which each of the two layers are laterally ordered just like in the monolayer and the particles in the second layer reside right above the interstitial sites of the hexagonally packed first-layer particles. It can be shown that when powder-averaged in two dimensions, $S_{2,C}(q_z)$ is given by

$$S_{2,C}(q_z) = [1 + 2 \sin^2(q_z l_{12}/2)] S_1(q_z), \quad (9)$$

where l_{12} is the vertical separation between the two layers. The factor multiplying S_1 in Eq. (9) arises from the two-particle basis across the two layers. The shown curve $S_{2,C}(q_z)$ has been calculated using the value $l_{12} = 29.0 \text{ \AA}$ determined by the fitting of the XR data (see Sec. III B).

It is clear from Fig. 10(d) that none of these extreme cases agree very well with the observed data. However, just as in the data, the curve $S_{2,C}$ based on interlayer correlations displays a maximum around $q_z \sim 0.1 \text{ \AA}^{-1}$. It should also be noted that if the nearest-neighbor distance *across* the two layers of the correlated bilayer were equal to the in-plane separation $a = 34 \text{ \AA}$, l_{12} would be equal to $l_{12} = (\frac{2}{3})^{1/2} a = 28 \text{ \AA}$, which is close to the XR-based value $l_{12} = 29.0 \text{ \AA}$. These observations suggest a certain degree of *cross* correlations between the short-range 2D hexagonal order in the two layers.

On the basis of these considerations, a better description of the actual state of the bilayer may be a mixture of both uncorrelated and correlated regions, such that $S(q_z)$ is described by a superposition between S_1 and $S_{2,C}$:

$$S_2(q_z) = c_1 S_1(q_z) + c_2 S_{2,C}(q_z), \quad (10)$$

where c_1 and c_2 are constants. As an example, the solid curve $S(q_z) = S_2(q_z)$ in Fig. 10(d) shows the case of $c_1 = 0.26$ and $c_2 = 0.41$. The intensity $I(\langle q_z \rangle)$ [crosses in Fig. 10(d)] calculated from this particular form of $S_2(q_z)$ roughly approximates the behavior of the observed Bragg-rod data. The fact that $c_1 + 2c_2 = 1.1$ is close to unity suggests that the number of AuSHDA particles *per unit surface area* that belong to hexagonally ordered domains is similar between the bilayer and the monolayer. Since this number for the bilayer is twice the number *per monolayer*, it is clear that the bilayer at A_5 consists of two monolayers each of which is less ordered than the monolayer at A_3 . As pointed out earlier in Sec. I, a similar disordering effect of monolayer collapse has also been observed in AuSCn and AgSCn Langmuir films ($-\text{CH}_3$ terminated particles).^{34,35} To summarize, the Bragg

rod data from the bilayer is consistent with the presence of local 2D hexagonal order within each of the two layers and also provides evidence for interlayer correlations of such order.

IV. SUMMARY

Langmuir films of gold nanoparticles derivatized with acid-terminated alkylthiol chains $[\text{HS}(\text{CH}_2)_{15}\text{COOH}]$ on acidic aqueous subphase ($\text{pH} = 3$) have been studied at room temperature. The Π - A isotherm of the AuSHDA Langmuir film exhibits a coexistence plateau that is consistent with a compression-induced monolayer/bilayer transition. The microscopic structures of AuSHDA films have been probed as a function of area/particle by using various surface-sensitive x-ray techniques. The results can be summarized as follows.

The electron density profiles extracted from the XR measurements are consistent with the formation of an AuSHDA monolayer on the low-density side of the coexistence plateau and a bilayer on the high-density side. The results of off-specular diffuse scattering measurements indicate that a close-packed monolayer near the onset of the transition is laterally homogeneous. Unlike the case of the monolayer, off-specular intensities scattered from a bilayer are higher than the values predicted from the presence of thermal capillary fluctuations and the assumption of homogeneity, providing evidence for the presence of lateral density inhomogeneities within the bilayer. The GID results show that upon being spread on the surface AuSHDA particles spontaneously aggregate into a 2D hexagonal structure with only short-range order. This structure is characterized by a nearest-neighbor distance of $a = 34 \text{ \AA}$ that is independent of the degree of lateral compression. The limited range of lateral order could be a consequence of the polydispersity in particle size. The Bragg rod of the lowest-order peak observed from a monolayer is consistent with a 2D array of Au cores. Subsequent compression across the coexistence plateau reduces the lateral order within the monolayer. The Bragg rod data from the bilayer suggests that some interlayer correlations exist between the lateral order of the two layers.

This study on Au nanoparticles had been motivated partly by the fact that they are very strong scatters of x rays due to their very high electron density. The results presented show that even though these particles only display short-range lateral order in the monolayer, the resulting lowest-order GID peak is intense enough to be easily observed. If some macromolecules can be synthesized such that they bear Au nanoparticles inside and their monolayers exhibit interesting compression- and/or temperature-dependent 2D phase behaviors, then, the Au particles should act as “markers” that would enable x-ray scattering studies of structural changes across order-disorder phase boundaries.

ACKNOWLEDGMENTS

We thank B. M. Ocko for helpful discussions. The Harvard contribution to this work was supported by Grant No. NSF-DMR-01-24936. R.B.L. acknowledges support from

NSERC. National Synchrotron Light Source at Brookhaven National Laboratory is supported by Grant No. DE-AC02-76CH0016.

- ¹M. G. Bawendi, M. L. Steigerwald, and L. E. Brus, *Annu. Rev. Phys. Chem.* **41**, 477 (1990).
- ²A. P. Alivisatos, *Science* **271**, 933 (1996).
- ³C. P. Collier, T. Vossmeier, and J. R. Heath, *Annu. Rev. Phys. Chem.* **49**, 371 (1998).
- ⁴S. Henrichs, C. P. Collier, R. J. Saykally, Y. R. Shen, and J. R. Heath, *J. Am. Chem. Soc.* **122**, 4077 (2000).
- ⁵G. Schmid, *Chem. Rev.* **92**, 1709 (1992).
- ⁶G. Schmid, M. Baumle, M. Geerkens, I. Helm, C. Osemann, and T. Sawitowski, *Chem. Soc. Rev.* **28**, 179 (1999).
- ⁷A. P. Alivisatos, P. F. Barbara, A. W. Castleman, *et al.*, *Adv. Mater. (Weinheim, Ger.)* **10**, 1297 (1998).
- ⁸A. N. Shipway, E. Katz, and I. Willner, *ChemPhysChem* **1**, 18 (2000).
- ⁹R. G. Freeman, K. C. Grabar, K. J. Allison, *et al.*, *Science* **267**, 1629 (1995).
- ¹⁰R. P. Andres, J. D. Bielefeld, J. I. Henderson, D. B. Janes, V. R. Kolagunta, C. P. Kubiak, W. J. Mahoney, and R. G. Osifchin, *Science* **273**, 1690 (1996).
- ¹¹R. P. Andres, T. Bein, M. Dorogi, S. Feng, J. I. Henderson, C. P. Kubiak, W. Mahoney, R. G. Osifchin, and R. Reifenberger, *Science* **272**, 1323 (1996).
- ¹²V. L. Colvin, M. C. Schiamp, and A. P. Alivisatos, *Nature (London)* **370**, 354 (1994).
- ¹³R. W. Siegel, *Sci. Am. (Int. Ed.)* **275**(6), 74 (1996).
- ¹⁴C. M. Niemeyer, *Angew. Chem., Int. Ed. Engl.* **40**, 4128 (2001).
- ¹⁵J. R. Heath, *Science* **270**, 1315 (1995).
- ¹⁶C. B. Murray, C. R. Kagan, and M. G. Bawendi, *Science* **270**, 1335 (1995).
- ¹⁷L. Motte, F. Billoudet, E. Lacaze, J. Douin, and M. P. Pileni, *J. Phys. Chem. B* **101**, 138 (1997).
- ¹⁸G. Schmid and L. F. Chi, *Adv. Mater. (Weinheim, Ger.)* **10**, 515 (1998).
- ¹⁹G. Schmid, M. Baumle, and N. Beyer, *Angew. Chem., Int. Ed. Engl.* **39**, 181 (2000).
- ²⁰J. H. Fendler and F. C. Meldrum, *Adv. Mater. (Weinheim, Ger.)* **7**, 607 (1995).
- ²¹V. L. Colvin, A. N. Goldstein, and A. P. Alivisatos, *J. Am. Chem. Soc.* **114**, 5221 (1992).
- ²²K. C. Grabar, P. C. Smith, M. D. Musick, J. A. Davis, D. G. Walter, M. A. Jackson, A. P. Guthrie, and M. J. Natan, *J. Am. Chem. Soc.* **118**, 1148 (1996).
- ²³K. V. Sarathy, P. J. Thomas, G. U. Kulkarni, and C. N. R. Rao, *J. Phys. Chem. B* **103**, 399 (1999).
- ²⁴A. Gole, S. R. Sainkar, and M. Sastry, *Chem. Mater.* **12**, 1234 (2000).
- ²⁵Z. L. Wang, *Adv. Mater. (Weinheim, Ger.)* **10**, 13 (1998).
- ²⁶Z. L. Wang, S. A. Harfenist, I. Vezmar, R. L. Whetten, J. Bentley, N. D. Evans, and K. B. Alexander, *Adv. Mater. (Weinheim, Ger.)* **10**, 808 (1998).
- ²⁷J. S. Yin and Z. L. Wang, *Phys. Rev. Lett.* **79**, 2570 (1997).
- ²⁸S. Connolly, S. Fullam, B. Korgel, and D. Fitzmaurice, *J. Am. Chem. Soc.* **120**, 2969 (1998).
- ²⁹P. C. Ohara, D. V. Leff, J. R. Heath, and W. M. Gelbart, *Phys. Rev. Lett.* **75**, 3466 (1995).
- ³⁰R. L. Whetten, J. T. Khoury, M. M. Alvarez, S. Murphy, I. Vezmar, Z. L. Wang, P. W. Stephens, C. L. Cleveland, W. D. Luedtke, and U. Landman, *Adv. Mater. (Weinheim, Ger.)* **8**, 428 (1996).
- ³¹K. V. Sarathy, G. Raina, R. T. Yadav, G. U. Kulkarni, and C. N. R. Rao, *J. Phys. Chem. B* **101**, 9876 (1997).
- ³²A. Taleb, V. Russier, A. Courty, and M. P. Pileni, *Phys. Rev. B* **59**, 13350 (1999).
- ³³C. J. Kiely, J. Fink, M. Brust, D. Bethell, and D. J. Schiffrin, *Nature (London)* **396**, 444 (1998).
- ³⁴J. R. Heath, C. M. Knobler, and D. V. Leff, *J. Phys. Chem. B* **101**, 189 (1997).
- ³⁵C. P. Collier, R. J. Saykally, J. J. Shiang, S. E. Henrichs, and J. R. Heath, *Science* **277**, 1978 (1997).
- ³⁶G. Medeiros-Ribeiro, D. A. A. Ohlberg, R. S. Williams, and J. R. Heath, *Phys. Rev. B* **59**, 1633 (1999).
- ³⁷S. H. Kim, G. Medeiros-Ribeiro, D. A. A. Ohlberg, R. S. Williams, and J. R. Heath, *J. Phys. Chem. B* **103**, 10341 (1999).
- ³⁸B. O. Dabbousi, C. B. Murray, M. F. Rubner, and M. G. Bawendi, *Chem. Mater.* **6**, 216 (1994).
- ³⁹F. C. Meldrum, N. A. Kotov, and J. H. Fendler, *Langmuir* **10**, 2035 (1994).
- ⁴⁰Y. C. Tian and J. H. Fendler, *Chem. Mater.* **8**, 969 (1996).
- ⁴¹M. Sastry, V. Patil, K. S. Mayya, D. V. Paranjape, P. Singh, and S. R. Sainkar, *Thin Solid Films* **324**, 239 (1998).
- ⁴²T. Torimoto, N. Tsumura, M. Miyake, M. Nishizawa, T. Sakata, H. Mori, and H. Yoneyama, *Langmuir* **15**, 1853 (1999).
- ⁴³K. S. Mayya, V. Patil, and M. Sastry, *Langmuir* **13**, 2575 (1997).
- ⁴⁴M. Sastry, K. S. Mayya, V. Patil, D. V. Paranjape, and S. G. Hegde, *J. Phys. Chem. B* **101**, 4954 (1997).
- ⁴⁵K. S. Mayya and M. Sastry, *J. Phys. Chem. B* **101**, 9790 (1997).
- ⁴⁶K. S. Mayya and M. Sastry, *Langmuir* **14**, 74 (1998).
- ⁴⁷K. S. Mayya, V. Patil, P. M. Kumar, and M. Sastry, *Thin Solid Films* **312**, 300 (1998).
- ⁴⁸M. Sastry, *Curr. Sci.* **78**, 1089 (2000).
- ⁴⁹K. S. Mayya and M. Sastry, *Langmuir* **15**, 1902 (1999).
- ⁵⁰A. Kumar, S. Mandal, S. P. Mathew, P. R. Selvakannan, A. B. Mandale, R. V. Chaudhari, and M. Sastry, *Langmuir* **18**, 6478 (2002).
- ⁵¹Y. Lin, H. Skaff, T. Emrick, A. D. Dinsmore, and T. P. Russell, *Science* **299**, 226 (2003).
- ⁵²G. Markovich, C. P. Collier, and J. R. Heath, *Phys. Rev. Lett.* **80**, 3807 (1998).
- ⁵³G. Markovich, C. P. Collier, S. E. Henrichs, F. Remacle, R. D. Levine, and J. R. Heath, *Acc. Chem. Res.* **32**, 415 (1999).
- ⁵⁴D. V. Leff, P. C. Ohara, J. R. Heath, and W. M. Gelbart, *J. Phys. Chem.* **99**, 7036 (1995).
- ⁵⁵M. Brust, M. Walker, D. Bethell, D. J. Schiffrin, and R. Whyman, *J. Chem. Soc., Chem. Commun.* **1994**, 801.
- ⁵⁶M. Brust, J. Fink, D. Bethell, D. J. Schiffrin, and C. Kiely, *J. Chem. Soc., Chem. Commun.* **1995**, 1655.
- ⁵⁷D. Bethell, M. Brust, D. J. Schiffrin, and C. Kiely, *J. Electroanal. Chem.* **409**, 137 (1996).
- ⁵⁸A. Badia, S. Singh, L. Demers, L. Cuccia, G. R. Brown, and R. B. Lennox, *Chem.-Eur. J.* **2**, 359 (1996).
- ⁵⁹A. Badia, W. Gao, S. Singh, L. Demers, L. Cuccia, and L. Reven, *Langmuir* **12**, 1262 (1996).
- ⁶⁰A. Badia, L. Cuccia, L. Demers, F. Morin, and R. B. Lennox, *J. Am. Chem. Soc.* **119**, 2682 (1997).
- ⁶¹H. Schmitt, A. Badia, L. Dickinson, L. Reven, and R. B. Lennox, *Adv. Mater. (Weinheim, Ger.)* **10**, 475 (1998).
- ⁶²M. M. Alvarez, J. T. Khoury, T. G. Schaaff, M. N. Shafiqullin, I. Vezmar, and R. L. Whetten, *J. Phys. Chem. B* **101**, 3706 (1997).
- ⁶³F. Remacle, C. P. Collier, J. R. Heath, and R. D. Levine, *Chem. Phys. Lett.* **291**, 453 (1998).
- ⁶⁴F. Remacle and R. D. Levine, *ChemPhysChem* **2**, 20 (2001).
- ⁶⁵D. K. Schwartz, M. L. Schlossman, and P. S. Pershan, *J. Chem. Phys.* **96**, 2356 (1992).
- ⁶⁶W. J. Foster, M. C. Shih, and P. S. Pershan, *J. Chem. Phys.* **105**, 3307 (1996).
- ⁶⁷G. M. Bommarito, W. J. Foster, P. S. Pershan, and M. L. Schlossman, *J. Chem. Phys.* **105**, 5265 (1996).
- ⁶⁸S. K. Sinha, E. B. Sirota, S. Garoff, and H. B. Stanley, *Phys. Rev. B* **38**, 2297 (1988).
- ⁶⁹M. K. Sanyal, S. K. Sinha, K. G. Huang, and B. M. Ocko, *Phys. Rev. Lett.* **66**, 628 (1991).
- ⁷⁰M. Fukuto, R. K. Heilmann, P. S. Pershan, J. A. Griffiths, S. M. Yu, and D. A. Tirrell, *Phys. Rev. Lett.* **81**, 3455 (1998).
- ⁷¹H. Tostmann, E. Dimasi, P. S. Pershan, B. M. Ocko, O. G. Shpyrko, and M. Deutsch, *Phys. Rev. B* **59**, 783 (1999).
- ⁷²P. S. Pershan, *Colloids Surf., A* **171**, 149 (2000).
- ⁷³M. Fukuto, Ph.D. thesis, Harvard University, Cambridge, 2001.
- ⁷⁴L. G. Parratt, *Phys. Rev.* **95**, 359 (1954).
- ⁷⁵J. Lekner, *Theory of Reflection* (Martin Nijhoff, Dordrecht, 1987).
- ⁷⁶M. Fukuto, R. K. Heilmann, P. S. Pershan, S. M. Yu, J. A. Griffiths, and D. A. Tirrell, *J. Chem. Phys.* **111**, 9761 (1999).
- ⁷⁷J. Als-Nielsen, D. Jacquemain, K. Kjaer, F. Leveiller, M. Lahav, and L. Leiserowitz, *Phys. Rep.* **246**, 251 (1994).
- ⁷⁸S. Dietrich and A. Haase, *Phys. Rep.* **260**, 1 (1995).
- ⁷⁹M. P. Gelfand and M. E. Fisher, *Physica A* **166**, 1 (1990).
- ⁸⁰P. S. Pershan, *Phys. Rev. E* **50**, 2369 (1994).
- ⁸¹I. M. Tidswell, T. A. Rabedeau, P. S. Pershan, and S. D. Kosowsky, *Phys. Rev. Lett.* **66**, 2108 (1991).